



**HAL**  
open science

# Continuous Recording of Viscoelastic Relaxation Processes at a Constant Ultrasonic Frequency Due To Wave-Induced Fluid Flow in a Microporous Carbonate Rock

Davide Geremia, Christian David

► **To cite this version:**

Davide Geremia, Christian David. Continuous Recording of Viscoelastic Relaxation Processes at a Constant Ultrasonic Frequency Due To Wave-Induced Fluid Flow in a Microporous Carbonate Rock. *Geophysical Research Letters*, 2021, 48 (19), pp.e2021GL095244. 10.1029/2021GL095244 . hal-03478858

**HAL Id: hal-03478858**

**<https://hal.science/hal-03478858>**

Submitted on 4 Apr 2022

**HAL** is a multi-disciplinary open access archive for the deposit and dissemination of scientific research documents, whether they are published or not. The documents may come from teaching and research institutions in France or abroad, or from public or private research centers.

L'archive ouverte pluridisciplinaire **HAL**, est destinée au dépôt et à la diffusion de documents scientifiques de niveau recherche, publiés ou non, émanant des établissements d'enseignement et de recherche français ou étrangers, des laboratoires publics ou privés.

## **Continuous recording of viscoelastic relaxation processes at constant ultrasonic frequency due to wave-induced fluid flow in a microporous carbonate rock**

**Davide Geremia<sup>1</sup>, and Christian David<sup>1</sup>**

<sup>1</sup>CY Cergy Paris Université, GEC, F-95000 Cergy, France.

Corresponding author: Davide Geremia ([davide.geremia@cyu.fr](mailto:davide.geremia@cyu.fr))

### **Key Points:**

- Viscoelastic relaxation processes were continuously recorded vs. time at fixed ultrasonic frequency in fluid substitution tests on chalk
- Increasing the water saturation above 80% induces a transition from relaxed to unrelaxed regime
- Johnson's model for patchy-saturated porous media accounts well for the observed P wave velocity and attenuation variations with saturation

**Abstract**

In a set of water injection, imbibition and drying tests on Obourg Chalk, relaxation processes induced by variations in water saturation were continuously recorded at constant ultrasonic frequency, with a peak in attenuation concomitant to a velocity increase from a lower to an upper bound. This behavior is well described by standard viscoelastic models, considering a continuously changing relaxation frequency which at water saturation above 80% matches the frequency of our ultrasonic pulse generator. Using a patchy saturation model, we show that heterogeneity in fluid distribution is responsible for this relaxation phenomenon which could be observed at ultrasonic frequency thanks to the very fine scale of the rock microstructure combining low permeability and high porosity. We believe that our detailed data set can feed new models or help improve existing ones for a better understanding of wave induced fluid flow processes in reservoir rocks.

**Plain Language Summary**

Relaxation processes were continuously recorded during experiments in which the fluid content in a porous rock was changing with time due to injection, evaporation or capillary processes. Significant variations in velocity and amplitude of compressive waves were observed and could be accounted for by models involving heterogeneous distributions of fluids at the microscopic scale. Such continuous recording of a relaxation transition, as predicted for example by viscoelasticity theory, was made possible in the range of frequency used in our experiments because of the very fine grain and pore size in the tested rock. Our data set will help geophysicists to improve the modelling of wave induced fluid flow in reservoir rocks.

**1 Introduction**

Monitoring of fluid motion in the crust is one of the most discussed topics in oil & gas applications as well as in geothermal systems and CO<sub>2</sub> storage. Detection of fluid migration is commonly done using seismic and sonic methods. In laboratory experiments, studies at ultrasonic frequencies remain the most effective way to highlight observations at large scale, because in such studies the boundary conditions are well constrained. However upscaling is an important part of the process for applications at the reservoir scale (Guéguen et al., 2006).

Regardless of their nature, fluids are proven to be associated with several dynamic effects on wave propagation at different scales, which generally depend on parameters such as pore size and structure. Generally, these phenomena can be grouped into the category of so-called wave-induced fluid flow (WIFF) processes (Müller et al., 2010). The presence of water in compliant pores like cracks for example, can produce overpressures responsible for wave dispersion, a mechanism known as squirt or local flow (Biot, 1956; G. Mavko & Jizba, 1991). Biot (1956) computed velocity dispersion based on inertial and viscous interactions between the fluid and the rock matrix (Mavko et al., 2009a). Dvorkin & Nur (1993) combined the latter into a unified Biot-Squirt (BISQ) model. Other approaches consider the increase in stiffness due to the dynamic pressure generated by a passing compressional wave on fluid filled pores and grain contact areas (Murphy et al., 1986; Tutuncu & Sharma, 1992), or the heterogeneity in fluid

distribution in partially saturated media causing flow between patches with different fluids (White, 1975).

Whereas many studies focused on the analytical description, few experimental efforts have been made to understand these phenomena. Recently many works on velocity dispersion and attenuation were conducted by varying the wave frequency over a broad range (Pimienta et al., 2015; Szewczyk et al., 2018) thanks to technological advances. Earlier studies focused on wave velocity measurements at fixed frequency while varying the degree of saturation. Among those, Murphy (1982a, 1982b) observed through measurements at seismic and ultrasonic wave frequencies a marked peak in attenuation and velocity variation both in the very low and high saturation ranges. This was attributed to moisture effects and wave induced fluid flow generating viscous dissipation. Le Ravalec et al. (1996) discussed the influence of fluid distribution during imbibition and drying on P-wave velocity: they stated that two parameters, related to how easily fluid patches can drain or saturate, are able to describe such processes. Cadoret et al. (1998), through drying and vacuum saturation tests on limestones, observed the formation of gas patches by CT scan associated with substantial attenuation. Lebedev et al. (2009a, 2009b) pointed out that at intermediate saturation, ultrasonic wave velocities are affected by the patch arrangement and size.

In our study, four kinds of experiments have been conducted at in-situ stress or room conditions to understand the mechanism of wave dispersion and attenuation at ultrasonic frequency: (1) Injection test with applied deviatoric stress, (2) injection test in hydrostatic conditions, (3) imbibition test and (4) drying test. In each experiment, we obtained a remarkable continuous recording of relaxation processes showing a transition from a relaxed regime, where the wave induced pressure has enough time to equilibrate, to an unrelaxed regime, where the pressure is not equilibrated and fluid flow can be neglected (Müller et al., 2010), with a substantial increase in P-wave velocity closely linked to a peak in attenuation. We believe that the designed experimental procedure, combined with the characteristics of the tested rock (i.e. grain and pore size) provided favorable conditions for the observation of a WIFF mechanism at fixed frequency, with fluid distribution as the only variable in the system.

## 2 Material, methods and results

The rock selected for this study is the Obourg chalk from Mons Basin (Belgium). It is a fine-grained microporous carbonate rock, formed during the Campanian age. It is composed mainly of calcite, with minor (less than 1%) clayey minerals (Faÿ-Gomord et al., 2016; Voake et al., 2019). Petrophysical properties of this rock are summarized as follows (average properties unless indicated): porosity 43%; water and gas permeability  $6.4 \times 10^{-16}$  and  $5 \times 10^{-15}$  m<sup>2</sup>, respectively; grain and bulk density 2720 and 1550 kg/m<sup>3</sup>, respectively; peak pore throat radius (mercury injection) 0.291 μm; peak grain radius (statistical image analysis on SEM pictures) 0.74 μm; P and S-wave velocities (dry samples) from 2200 to 2700 m/s for P-wave and from 1400 to 1500 m/s for S-wave (Geremia et al., 2021). The matrix of this chalk is mainly composed of coccoliths fragments with punctic contacts and a large inter and intraparticle porosity, making the pore space open and well connected (Faÿ-Gomord et al., 2016, 2017; Geremia et al., 2021). The degree of cementation is low. The tests were conducted on cylindrical cores 80 x 40 mm, machined from blocks collected in the Harmignes quarry (South of Mons

city). The datasets used in this study are accessible at <https://doi.org/10.6084/m9.figshare.14959608.v1>.

## 2.1 Injection tests under stress

A detailed description of the experimental setup can be found in the Supporting text S1 and in Geremia et al. (2021). We performed an ultrasonic survey during water injection into rock samples with six P-wave piezoelectric transducers (PZTs) distributed as shown in Figure 1, allowing us to measure the flight time and the first peak amplitude of the recorded signals.

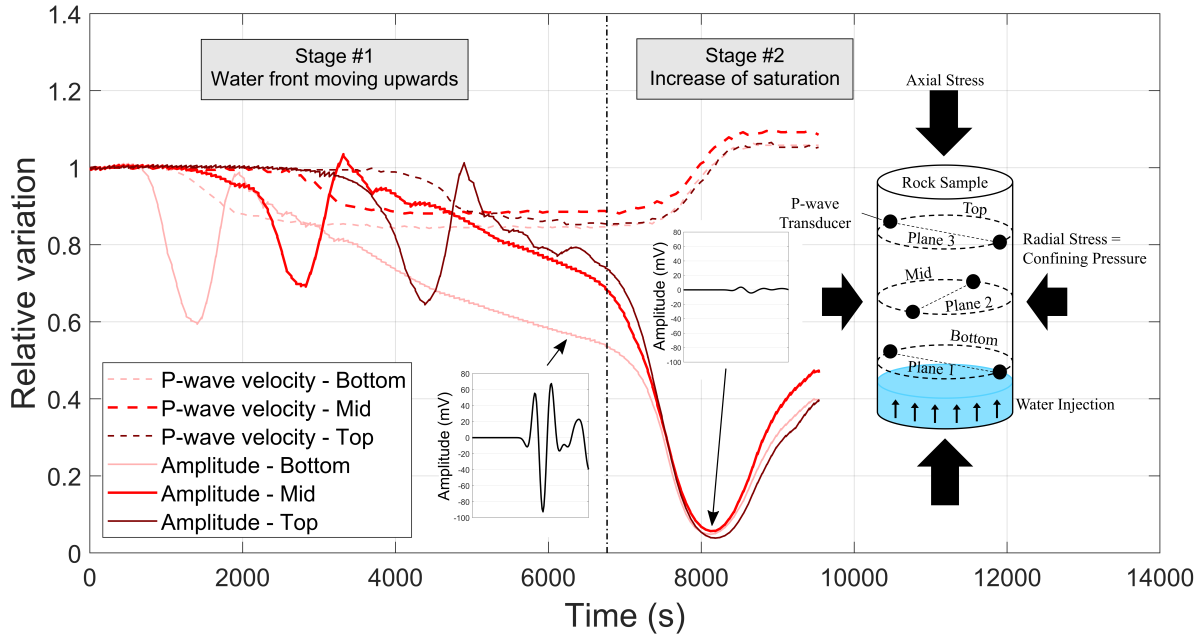


**Figure 1.** Evolution of P wave velocity and amplitude normalized to their value in the dry state before the start of water injection. The sample is Obourg Chalk OB15-65 tested at 1.5 MPa confining pressure and 6.5 MPa differential stress. A sketch of the PZT sensors assembly on the rock sample is also shown. A very large drop in the waveform amplitude is observed at the peak of relaxation.

We conducted several injection tests at differential stresses between 6.5 and 7.5 MPa, the aim of which was to relate the applied stress and the amount of injected water needed to cause failure through water-induced weakening (Geremia et al., 2021). In the current work, we only focus on the evolution of P-wave velocity ( $V_P$ ) and amplitude ( $A_P$ ) associated with water saturation. The different injection tests are named as follows, OBXX-YY with OB for Obourg chalk, XX for the applied confining pressure and YY for the applied differential stress, both with units in Bar ( $10^5$  Pa). Figure 1 shows the variations of the observed  $V_P$  and  $A_P$  normalized to their value at the start of water injection on the three horizontal paths (plane 1, 2 and 3) for test OB15-65.

For both parameters, we observe a sequential change from bottom to top (stage #1) following the upward rise of the water. Such an evolution of the P wave attributes during the rise of the water front has been analyzed in our previous works (David et al., 2015a, 2017a, 2017b).

In these studies, a decoupling between amplitude and velocity variations was already observed for that stage, with the decrease in  $A_P$  occurring before the  $V_P$  one. A review of possible explanations for such behavior has been proposed by Pimienta et al. (2019). Focusing here on stage #2 where the water front is well above the height of all ultrasonic sensors, we observe that  $V_P$  increases simultaneously in the three planes, while  $A_P$  goes through a minimum. Indeed the S-shape evolution of P-wave velocity matches a peak in attenuation, a property commonly found in systems where relaxation processes are taking place, such as in viscoelasticity. There is a striking synchronicity in our observations on all sensors planes, showing that the observed variations are linked to a bulk change in the rock rather than to a propagating event, like in stage #1. Examples of recorded waveforms are also displayed in Figure 1, one before the strong increase in attenuation and one exactly at the peak. Similar observations found for other injection tests conducted at different differential stresses (OB15-68 at 6.8 MPa and OB15-73 at 7.3 MPa) are shown in Figure 2a.

In order to check if the results of our injection tests were related to the differential stress applied in those tests, a water injection test under hydrostatic conditions was conducted as well. The term hydrostatic refers here to an injection test with no differential stress applied, at the same confining pressure of 1.5 MPa. Water was injected with the same pore pressure gradient as for the previously described injection tests and the water saturation reached at the end of the test was about 98%. Once again, the sample was instrumented with six PZTs in the same configuration as for the injection tests. It displays the same attributes as for the injection tests under deviatoric stress (Figure 2c). However, the peak-like shape of attenuation is not symmetrical as the amplitude is recovering very slowly after reaching a minimum value. This may be caused by the fact that, under deviatoric conditions, the effective mean stress  $(\sigma_1 - 2\sigma_3)/3$  is much higher than in hydrostatic condition, which may cause (1) signal enhancement and/or (2) the saturation to be close to 100%.

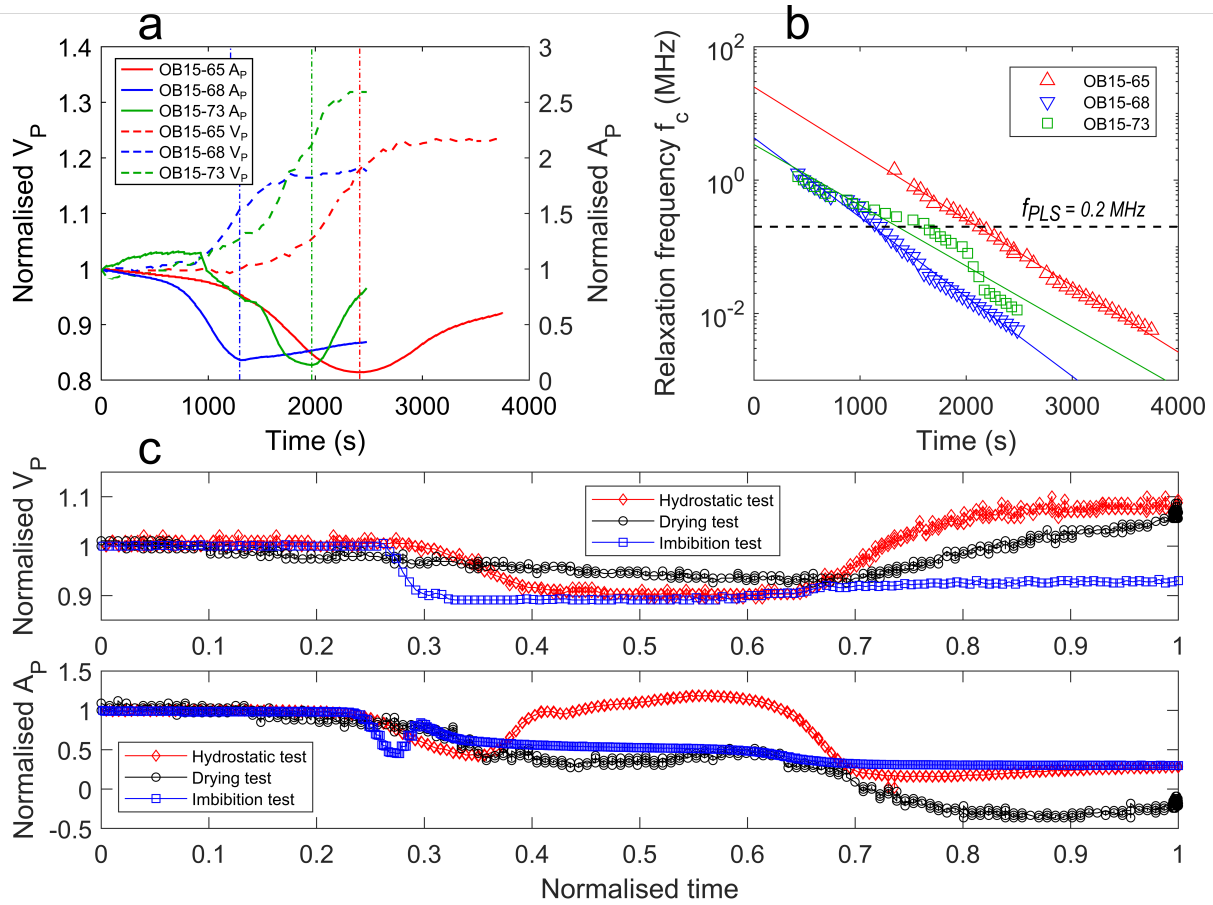


**Figure 2.** a) Results for three injection tests at different deviatoric stresses for stage #2 only, showing similar features as in Fig. 1. b) Relaxation frequency shift with time as estimated through the Zener viscoelastic model. c) Normalized P-wave velocity and amplitude evolution vs. time for the injection test under hydrostatic loading, and for the drying and imbibition tests at room conditions. For the drying test, data are displayed in reversed time order to be compared with the other data sets, i.e. the evaporation starts at relative time 1 and ends at 0 (the experiment proceeded from right to left).

## 2.2 Imbibition and drying tests at room conditions

An imbibition test was conducted with the same procedure as in David et al. (2015a). The rock sample is suspended under an electronic balance to register the sample mass increase during spontaneous capillary rise. A digital camera records the water rise at the sample surface during the test. The water is kept permanently in contact with the bottom end of the sample. The same PZTs configuration and processing scheme as for the injection test were used. The two stages observed in the injection tests are also recognizable in the imbibition test (Figure 2c); however, the  $V_P$  in stage #2 does not experience a sharp increase like we observed in Figure 1, whereas the amplitude just slightly decreases. This different behavior is likely due to the air trapped in the pore space which prevents complete saturation. The imbibition test provides however the

opportunity to relate the waterfront position with the change in  $V_P$ . We used this criterion to obtain the water height as a function of time inside the pressure vessel so that we could compute the water saturation (Supporting Text S2).

Once the hydrostatic test described in the previous section was completed, the rock sample was quickly removed from the pressure vessel and immediately suspended under an electronic balance in order to measure the sample mass decrease with time during drying under room conditions. As for the mechanical tests, the waveforms were recorded with 6 PZTs. The rock sample took approximately 3 days to return to the initial dry mass. Nevertheless, once more they display the same peak in attenuation correlated with the variation in P-wave velocity (Figure 2c). However it is important to note that the time scale for the drying test (several days) is significantly larger than the one for the mechanical tests (several hours).

### 3 Discussion

In our experimental data, it is possible to split the velocity-amplitude vs. time data sets in two parts (Figure 1); in stage #1 the P-wave velocity decreases and the first peak amplitude undergoes a fluctuation as a result of the upward motion of the water front, followed by stage #2 where the  $V_P$  increases and  $A_P$  experiences a peak in attenuation. The amplitude oscillation observed in the first stage can be induced by a superposition and interference of the direct wave and a reflected wave onto the moving waterfront (David et al., 2018; Kovalyshen, 2018).

Here we focus on stage #2, where the attenuation peak correlates with the  $V_P$  inflection point. We believe that our experimental data set shows the onset of relaxation processes, marked by a shift from a relaxed regime towards an unrelaxed one with time, at a constant frequency. We postulate that such relaxation processes can be explained by variations in the fluid distribution inside the rock samples during injection, imbibition or drying. In the past, several models for frequency dispersion and attenuation have been developed based on theories like poroelasticity (Biot, 1956; Bourbié et al., 1987; Pride, 2005), on pressure relaxation effects between compliant and stiff pores (e.g. squirt flow, (Mavko & Nur, 1975)) or on viscoelastic relaxation processes. Such a behavior, involving the passage from a low velocity limit to a high velocity limit concomitant with a peak in attenuation is well described by classical viscoelastic models: using the outcome of the standard linear solid (or Zener) model for the evolution of velocity and attenuation in the vicinity of the relaxation frequency, we found that our data set is consistent with an exponential decrease of the relaxation frequency with time, thus with water saturation, intercepting the pulsing frequency  $f_{PLS} = 0.2$  MHz of our ultrasonic device (Figure 2b). Given this result, it is reasonable to link the observed behavior to a frequency-dependent mechanism induced by the progressive saturation and the evolving fluid distribution in the pore space.

Several models have been proposed to account for wave dispersion and attenuation in fluid bearing porous media, allowing for the calculation of the critical frequency at maximum attenuation from fluid- or matrix-related parameters. The outcome of some of these models for the prediction of the relaxation frequency is discussed in Supporting text S3 from which we concluded that among these, the patchy saturation model introduced by White (1975) represents the most suitable one. Indeed, for the Obourg chalk (i) the critical frequency for the drained to undrained transition is 2.3 Hz and (ii) the critical frequency for the transition from (undrained)

relaxed to unrelaxed regime through the squirt flow model requires a crack aspect ratio far too small to be consistent with our ultrasonic measurements. Conversely, the patchy saturation model is based on relaxation phenomena triggered by fluid heterogeneities in rocks, which are likely to develop during water injection, and considers pockets of one fluid (in our case air) distributed across a medium saturated with a second fluid (in our case water). Kobayashi & Mavko (2016) explored the variation of patch size as a function of saturation. For a critical frequency equal to  $f_{PLS}$ , the patchy saturation model requires an elementary patch size of nearly 50  $\mu\text{m}$  (Supporting text S3), which is approximately two orders of magnitude higher than the pore size ( $\approx 0.3 \mu\text{m}$ ) and three orders of magnitude lower than the wavelength ( $\approx 11 \text{mm}$ ). In White's model (White, 1975), compressional waves induce oscillatory fluid flow across the boundary between both fluids and, consequently, a loss of energy. The patchy saturation model was improved to make it consistent with the Biot poroelasticity theory (Dutta & Odé, 1979a, 1979b; Vogelaar et al., 2010). In the following we adopted the formalism proposed by Johnson (2001, 2007), hereafter referred to as Johnson's model, who developed a patchy saturation model in the low-frequency limit of the Biot theory. Indeed, for Obourg chalk the Biot crossover frequency (Johnson, 2001) is  $f_B = 76 \text{MHz}$  so that our data set at ultrasonic frequency belongs to the low-frequency regime of the Biot poroelasticity theory. In this regime viscous effects dominate, and the slow Biot wave is a diffusion wave with a wavelength of 54  $\mu\text{m}$  much smaller than the fast P-wave wavelength (Müller et al., 2010). We checked that Johnson's model yields negligible errors with respect to the exact solution provided by Vogelaar et al. (2010). In the low and high frequency limit the bulk modulus tends to the Gassmann-Wood ( $K_{GW}$ ) and Gassmann-Hill ( $K_{GH}$ ) effective moduli respectively. In the intermediate frequencies, the complex bulk modulus ( $K^*$ ) as a function of angular frequency  $\omega$  is computed by:

$$K^*(\omega) = K_{GH} - \frac{K_{GH} - K_{GW}}{1 - \zeta + \zeta \sqrt{1 - \frac{i\omega\tau}{\zeta^2}}} \quad (1)$$

where  $\zeta$  and  $\tau$  are two parameters depending on the size and the surface to volume ratio of the patches (Johnson, 2001; Müller et al., 2010). Shear modulus variations with frequency and saturation are not considered.

In all the tests performed on chalk, due to the experimental configuration, heterogeneities in the air-water distribution are spread across the rock sample before full saturation. The elementary volume in the model is an outer water saturated sphere of radius  $b$  which surrounds an inner air-filled sphere of radius  $a$ . The characteristic length scale for interactions between patches is  $L_p = b - a$ . Changing the patch size at a fixed wave frequency will allow a transition from the relaxed towards the unrelaxed regime. It is important to note that in nature, the size and shape of the heterogeneities ( $a$  and  $b$ ) should be described by a range of values rather than a unique one: for the sake of simplicity, we stick to the periodic spherical model initially introduced by White (1975). To determine the heterogeneity size, we computed the P-wave dispersion and attenuation as a function of frequency with Johnson's formulation and, by assigning a range of  $b$  values we compared the results to the experimental data using a trial-and-error method. This yielded a value  $b = 63 \mu\text{m}$  of the same order as the patch length derived from the theoretical relaxation frequency (Supporting text S3). This value for  $b$  was kept constant although in reality

both  $a$  and  $b$  probably vary, but since we do not have any control over these parameters, we chose to vary only one of them. Moreover, in isotropic rocks, the pressure gradient generated by a passing wave on these fluid patches is controlled by the fluid-diffusion relaxation scale  $L_d$  defined as:

$$L_d = \left( \frac{kK_f}{\eta\phi f} \right)^{1/2} \quad (2)$$

which depends on porosity, permeability, fluid viscosity  $\eta$ , fluid bulk modulus  $K_f$  and frequency  $f$ . If the patch size  $L_p$  is larger than  $L_d$ , the pressure gradient between different patches has not enough time to equilibrate. For Obourg chalk,  $L_d$  is equal to 120  $\mu\text{m}$  which is also in the same range as the previously mentioned value. Given these results, both the wavelength of the Biot slow wave and the patch size are much smaller than the wavelength of the fast P-wave and, for this reason, we proceeded by implementing the best choice value  $b = 63 \mu\text{m}$  as the radius of the outer sphere in Johnson's model. We computed the P wave dispersion and attenuation from the calculation of the complex bulk modulus (equation 1) as a function of water saturation by changing the radius  $a$  of the inner sphere (gas pocket) from  $a = b = 63 \mu\text{m}$  to  $a = 0$ , in a frequency range from  $10^2$  to  $10^{10}$  Hz. The water saturation is computed as  $S_w = 1 - (a/b)^3$ . Doing so, we map out the real part (linked to velocity dispersion, Figure 3a) and imaginary part (linked to attenuation, Figure 3b) of the complex bulk modulus as a function of frequency and saturation.

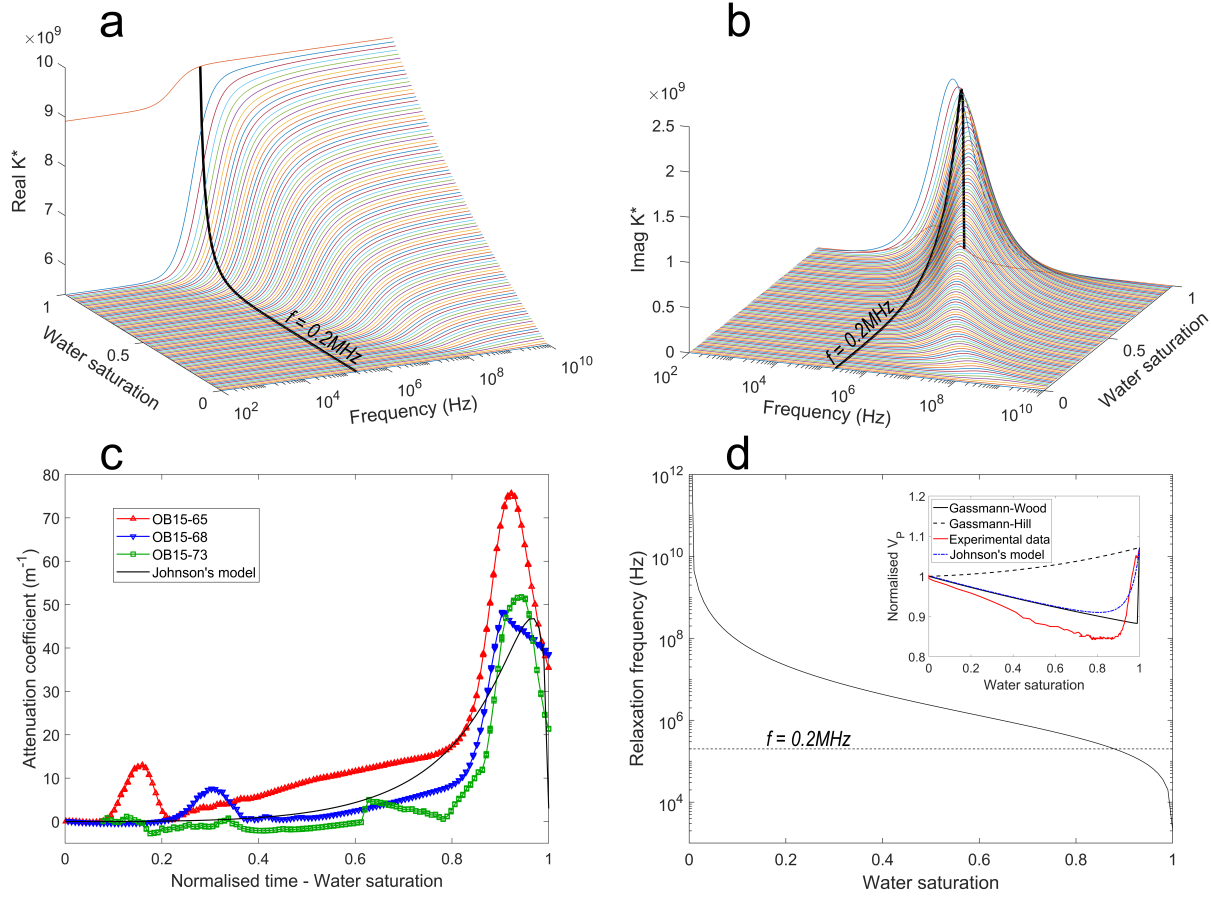


**Figure 3.** Prediction of the patchy saturation model (Johnson, 2001) for the evolution of the complex bulk modulus vs. frequency and saturation: a) Real part and b) Imaginary part. c) Comparison of Johnson's model with experimental data for the attenuation coefficient. d) Variation of the relaxation frequency for the patchy saturation model vs. water saturation and velocity evolution vs. water saturation for effective medium models and experimental data.

At fixed water saturation, the model reproduces well a peak in attenuation and the S-shape of the bulk modulus (from which the P wave velocity is inferred) as a function of frequency. At fixed frequency a peak in attenuation is observed when varying water saturation: when the frequency increases, the peak in attenuation and the velocity dispersion are smaller and occur at lower values of saturation. The path followed at fixed frequency  $f = f_{PLS}$  has been drawn on Figures 3a and b. The computed results along the black line in Figure 3b allow us to calculate in Figure 3c the attenuation coefficient predicted by Johnson's model at  $f = f_{PLS}$  as a function of saturation, which successfully matches the experimental data both qualitatively and quantitatively, where the attenuation coefficient  $\alpha$  is computed as:

$$\alpha = - \left( \frac{\ln \left( \frac{A_t}{A_0} \right)}{d} \right) \quad (3)$$

with  $A_t/A_o$  the ratio between the amplitude at time  $t$  and the initial amplitude, and  $d$  the distance between the emitter and receiver. Note that, while Johnson's model is in water saturation domain, the experimental tests are in normalized time domain, revealing that water saturation increases from 0 to a nominal saturation close to 1 with time. The smaller peaks in attenuation occurring at early times (low saturation) are related to stage #1 (water front rise) and can obviously not be accounted for by Johnson's model. By increasing the water saturation, the critical frequency at the relaxed-to-unrelaxed transition decreases (Figure 3d) and the peak in attenuation moves toward lower frequencies, which is in good agreement with the prediction of the viscoelasticity model in Figure 2b (see also the movie in the Supporting Information).

The P-wave velocity computed from Johnson's model is compared to the experimental data from test OB15-65 in the insert of Figure 3d (top right corner), for which the water saturation is calculated as explained in Supporting text S2. For comparison, the prediction of Gassmann-Wood and Gassmann-Hill limits (Müller et al., 2010) are also displayed. At lower saturation, the experimental results seem to match the Gassmann-Wood prediction, whereas, at higher saturation, a deviation from this trend leads toward the Gassmann-Hill model. The mismatch in the saturation value at the onset of velocity increase which occurs at  $S_w = 85\%$  compared to 98% modelled with Gassmann-Wood has also been observed by Lebedev et al. (2009a) on Casino sandstone. They explained such behaviour by variations in the patch arrangement and size which lead the velocity to switch from the Gassmann-Wood to the Gassmann-Hill limits. A similar behavior has been described by Cadoret et al. (1995, 1998) where a departure of the P-wave velocity from the Gassmann-Wood limit is explained by heterogeneities in the fluid distribution. Unfortunately, our modelling does not provide any information about the formation of the patches and their possible merging. Probably a different combination of sample size, rock microstructure and experimental procedure will affect the shape and size of the air pockets which could be analyzed in a further work through imaging techniques. Figure 3d shows that our experimental data are qualitatively similar to the prediction of Johnson's model; in addition, we believe that the lower velocities measured in our experiment (by about 7% at 80% of saturation) and the higher peak in attenuation (Figure 3c) can result from the "water weakening effect" in Obourg chalk (Geremia et al., 2021). Indeed, chemical or surface effects on the grain contact area are known to affect the mechanical properties of rocks and the magnitude of the P-wave velocity passing from dry to water-saturated conditions (Murphy, 1984), which are not accounted for by Johnson's patchy saturation model.

## 4 Conclusions

In the present work we showed that fluid heterogeneities can be the cause of significant variation in P-wave velocity and attenuation during water saturation in the microporous Obourg chalk. An almost continuous recording of relaxation processes linked to variations in fluid saturation at fixed ultrasonic frequency was obtained. We believe that such a continuous recording of relaxation processes can feed new models or help to improve existing ones for a better understanding of wave induced fluid flow processes in reservoir rocks.

The observed behavior is similar to the relaxation processes in classical viscoelasticity models like the standard linear solid or Zener model. Indeed at saturation above 80% a transition

from relaxed to unrelaxed regimes occurs, as the relaxation frequency, decreasing with saturation, matches at some point the frequency of the pulsing system used in the experimental setup. Application of effective medium models demonstrates that as saturation increases, the system undergoes a transition from the Gassmann-Wood (or isostress) to the Gassmann-Hill (or patchy) behaviour. By applying Johnson's (2001, 2007) formulations for patchy saturation, we have been able to fit the experimental data. This result shows that, within the measurement errors, the spherical shell model originally proposed by White (1975) for patchy-saturated porous media is relevant and accurate enough for the microporous Obourg chalk.

The size of the patches, in Johnson's model, was of the order of 50  $\mu\text{m}$ , which is larger than the pore scale ( $\approx 0.3 \mu\text{m}$ ) but lower than the wavelength of the fast P wave ( $\approx 11 \text{ mm}$ ). It is very likely that (i) the very fine scale of the rock microstructure combining small pore size, low permeability and high porosity, and (ii) the way fluids are distributed in the experimental setup both permit this relaxation phenomenon to be observed at ultrasonic frequency. Nevertheless, the same kind of mechanisms might take place in wave-induced fluid flow occurrence at a larger scale and at seismic frequencies, even in the same type of rock, as long as the condition of patch scale lower than the wavelength is fulfilled.

The results gained from this work provide new insights into the mechanisms acting during water injection or fluid substitution in rocks and, for this reason, they can contribute to a better understanding of seismic monitoring of a reservoir during secondary or tertiary recovery.

### **Acknowledgments**

Many thanks to both reviewers and to the editor for their advices which helped us to significantly improve our work. This work has been funded by the GEO<sup>2</sup>FRIP<sup>2</sup>SK project granted by the Initiative d'Excellence Paris Seine at CY Cergy Paris Université. DG is grateful to the Ecole Doctorale Sciences et Ingénierie who granted his PhD fellowship. This work has benefited from discussions with Beatriz Menéndez and Christophe Barnes, co-advisors of DG. Fruitful collaborations with our project partners at Université de Mons and CSIRO Perth are acknowledged. Many thanks to Laurent Louis for his careful reading of the final version.

### **Data Availability Statement**

The data supporting this work are available at <https://doi.org/10.6084/m9.figshare.14959608.v1>.



*Geophysical Research Letters*

Supporting Information for

**Continuous recording of viscoelastic relaxation processes at constant ultrasonic frequency due to wave-induced fluid flow in a microporous carbonate rock**

Davide Geremia and Christian David

CY Cergy Paris Université, GEC, F-95000 Cergy, France.

**Contents of this file**

Text S1 to S3  
Figures S1

**Additional Supporting Information (Files uploaded separately)**

Caption for Movie S1

**Introduction**

In the following, the supporting material is divided into three sections:

1. We describe the involved experimental setup and the protocol for the different tests.
2. We explain how we measured the water saturation as a function of time through the imbibition test and how this information is used in the injection tests.
3. We analyze different theories for wave dispersion and attenuation to identify the origin of the recorded relaxation processes.

**Text S1: Experimental setup, injection test protocol and complementary data set**

A Sanchez Technologies™ pressure vessel mounted on a GDS Instruments Ltd™ VIS loading frame with servo-controlled axial displacement were used for all the mechanical tests. The core sample is placed inside a neoprene sleeve through which we connected six P-wave piezoelectric transducers (PZTs) with 5 mm in diameter emplaced in a brass holder. The sensors are either glued or simply pushed in contact with the sample using an ultrasonic couplant gel. The sensors are distributed in three planes at different heights, named bottom, mid and top, as shown in the sketch in Figure 1, allowing for the measurement of P-wave velocity (called  $V_p$  hereafter) and for the recording of waveforms in 15 different pathways. For the purpose of this work, only the horizontal/radial  $V_p$  has been considered.

An AMSY-5 Vallen Systeme GmbH (Germany) was used to operate with the sensors in active mode. An ultrasonic survey proceeds by switching each sensor between pulser and receiver. The pulsing frequency imposed during velocity surveys is  $f_{PLS}=0.2$  MHz and the voltage amplitude sent to the emitter is about 100 Volts. Four repeated pulsing cycles are conducted per sensor giving a total of 144 recorded waveforms (6 received signals, times 4 pulses, times 6 sensors). We applied a time interval between each survey of 45 to 60 seconds.

The P-wave first arrival time is picked automatically through the Akaike Information Criterion (AIC) (Leonard & Kennett, 1999) which has proved very effective in discarding the possible noise located before the real signal. The  $V_p$  is computed by applying a calibrated distance matrix knowing the sample dimensions and the sensors positions. No corrections were made for the change in travel path lengths due to strain during the experiments since we found this effect to be negligible. In addition to  $V_p$ , the P-wave first peak amplitude (called hereafter  $A_p$ ) was also automatically measured in a time window after the P-wave first arrival.

An injection test is carried out following the novel procedure of David et al. (2015b) and adopted in Geremia et al. (2021a). After applying a target differential stress ( $\sigma_{\text{axial}} - \sigma_{\text{radial}}$ ) below the yielding point of the rock and a period of stabilization from 30 to 60 minutes, water injection is started, as shown in the top right sketch in Figure 1, with a bottom pore pressure of 0.12 MPa, while vacuuming from the top in order to avoid as much as possible air trapping in the pore space (giving a pore pressure difference of about 0.2 MPa from bottom to top). The described procedure permits to reach a nominal full saturation of the rock sample at the end of the experiment.

### **Text S2: Estimation of water saturation through imbibition test**

The imbibition tests give the possibility to link the waterfront position at the surface with the variation in  $V_P$ . For the imbibition test, a drop in  $V_P$  of about 10% induced by the rising water is observed in stage #1. This behaviour is observed in all travel paths and takes place systematically when the waterfront is about  $5 \text{ mm} \pm 1 \text{ mm}$  below the plane containing the PZTs. This distance is measured accurately on the pictures of the sample surface taken every second by the camera. This criterion can be used to infer the waterfront position as a function of time for the injection tests in which we record the  $V_P$  decrease due to the rising water while we do not see the sample in the pressure vessel. Subsequently, we consider that the water-invaded area is not homogeneously saturated, and, for this reason, we modelled a water saturation profile from the bottom to the top of the area reached by the water. For instance, let us assume in Figure S1 that the water reached approximately the first centimeter of the rock sample, then the black line shows the fluid distribution. The known parameters are the height reached by the water and the total volume injected. With an iterative process, we match this volume with the area below the distribution profile. This is reproduced for each position step and the results give a rightward and upward movement of the distribution profile as shown on the bottom left corner of Figure S1.

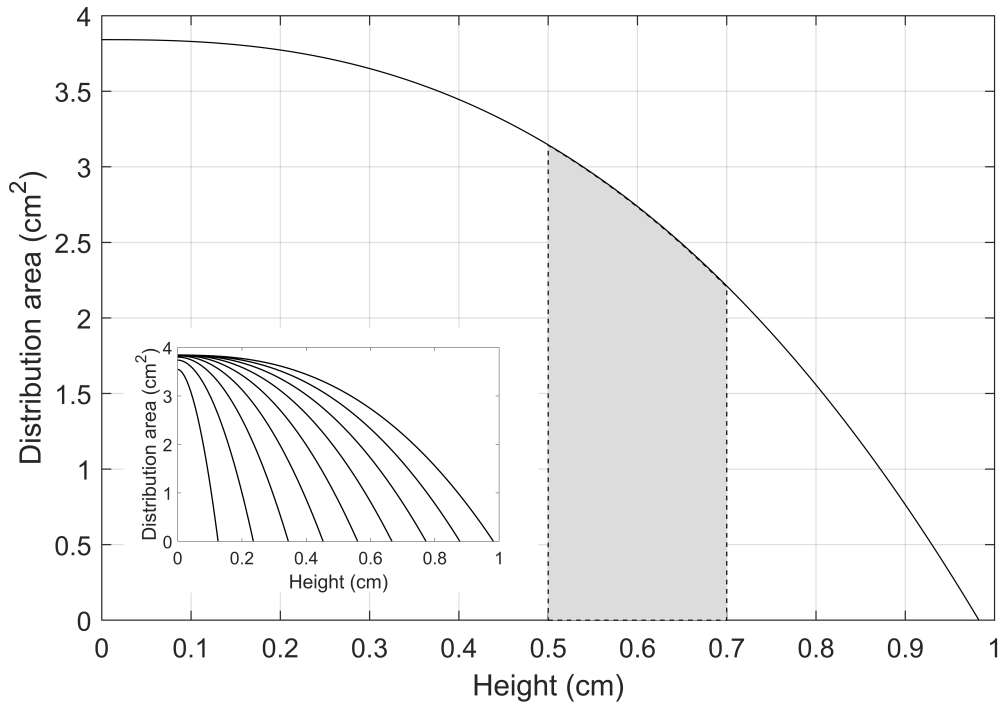


**Figure S1.** Estimated water saturation profile behind the water front position derived from the imbibition experiment. Example of water distribution during injection at the moment when the water front is at 0.98 cm from the bottom of the rock sample. The saturation decreases from the bottom to the top of the water invaded area. In the lower left corner, the distribution for nine consecutive times during injection is shown.

Hence, we can estimate the water saturation in any particular region of the sample like the grey area between 0.5 and 0.7 cm in Figure S1, from the volume given by the integral of the distribution profile, divided by the pore volume. With this criterion, the error in the estimated water saturation follows a power law with increasing the height of the water-invaded area. For instance, for any pore volume injected into 5 cm of the rock sample, the error in the water saturation is 1.53%.

**Text S3: Identification of the relaxation process**

Poroelasticity theory predicts a transition from a drained regime to an undrained one at a critical or cut-off frequency  $f_c^{(poro)}$  depending on the permeability  $k$ , the dry bulk modulus  $K_d$ , the fluid viscosity  $\eta_f$  and the sample length  $L_s$  (Cleary, 1978; Pimienta et al., 2015). For frequencies higher than  $f_c^{(poro)}$  the undrained regime is isobaric or relaxed, but another relaxation transition can occur between this relaxed regime and an unrelaxed one where pore pressure is heterogeneously distributed. Squirt flow can account for this relaxation process through local flow either from compliant cracks to stiffer pores (O'Connell & Budiansky, 1977) or from compliant grain contacts to pores (Murphy et al., 1986): the corresponding critical frequency  $f_c^{(s squirt)}$  depends on the fluid viscosity, the dry bulk modulus and on the aspect ratio  $\xi$  of the compliant elements. White (1975) introduced a model for the relaxed-unrelaxed transition based on patchy saturation, which requires the porous media to be partially saturated, with discrete patches of one fluid (e.g. air) embedded in a medium saturated with a second fluid (e.g. water). The critical frequency  $f_c^{(patchy)}$  for this mechanism depends on the permeability, the water viscosity (for patches made of air embedded into water), the patch size  $L_p$  and an effective bulk modulus  $K_E$  (White, 1975) depending on water, matrix and dry bulk moduli and porosity. A complete (but lengthy) definition of  $K_E$  can be found in Carcione et al. (2003). Finally the Biot crossover frequency  $f_c^{(Biot)}$  depending on the porosity  $\phi$ , the fluid density  $\rho_f$  and viscosity, the permeability and the tortuosity  $T$  features a transition between a regime dominated by viscous forces towards a regime where inertial forces decouple the fluid from the solid motion (Johnson, 2001). The critical frequencies for these relaxation processes are given in Equation S1.

$$f_c^{(poro)} = \frac{4kK_d}{\eta_f(L_s)^2}; f_c^{(s squirt)} = \frac{\xi^3 K_d}{\eta_f}; f_c^{(patchy)} = \frac{kK_E}{\pi\eta_f(L_p)^2}; f_c^{(Biot)} = \frac{\eta_f\phi}{2\pi k\rho_f T} \quad \text{Eq. S1}$$

Taking  $k = 6 \cdot 10^{-16} \text{ m}^2$ ,  $K_d = 6.1 \cdot 10^9 \text{ Pa}$ ,  $L_s = 0.08 \text{ m}$  for our Obourg Chalk samples and  $\eta_f = 0.001 \text{ Pa}\cdot\text{s}$ , we get  $f_c^{(poro)} = 2.3 \text{ Hz}$ , which shows that the recorded relaxation processes are clearly not linked to the drained-undrained transition. Taking  $\rho_f = 1000 \text{ kg/m}^3$ ,  $T \sim 1.5$  and  $\phi = 0.43$  for Obourg chalk yields  $f_c^{(Biot)} = 76 \text{ MHz}$ , showing that our measurements are done in the low frequency limit for the Biot relaxation. For the squirt flow mechanism, a crack aspect ratio  $\xi = 3.2 \cdot 10^{-3}$  is needed to obtain a critical frequency equal to  $f_{PLS} = 0.2 \text{ MHz}$ , which according to our microstructure analysis (Geremia et al., 2021a) seems unrealistic. For the patchy saturation mechanism, taking  $K_E = 2.9 \cdot 10^9 \text{ Pa}$  for Obourg chalk, a patch length  $L_P = 53 \text{ }\mu\text{m}$  is required to get a critical frequency equal to  $f_{PLS} = 0.2 \text{ MHz}$ , which is approximately two orders of magnitude higher than the pore size ( $\approx 0.3 \text{ }\mu\text{m}$ ) and three orders of magnitude lower than the fast P wave wavelength ( $\approx 11 \text{ mm}$  considering  $V_P = 2250 \text{ m/s}$  for our rock). This result makes the patchy saturation model the most realistic one.

**Movie S1.** The movie explains how the process of decreasing in critical frequency with water saturation can affect the attenuation and dispersion observed in the experimental data. The Critical frequency  $f_c$  in between the relaxed and unrelaxed regimes, moves to lower frequencies intercepting the pulsing frequency of the PZTs used in the experiments, causing a peak in attenuation and an increase in bulk modulus and velocity.